IEEE Access
Multidisciplinary | Rapid Review | Open Access Journal

Received December 6, 2018, accepted January 5, 2019, date of publication January 14, 2019, date of current version February 14, 2019.

Digital Object Identifier 10.1109/ACCESS.2019.2892766

Reference Layer Artefact Subtraction (RLAS): Electromagnetic Simulations

MUHAMMAD E. H. CHOWDHURY[1], (Member, IEEE), AMITH KHANDAKAR[1], (Senior Member, IEEE), KAREN MULLINGER[2,3], BELAYAT HOSSAIN[4], (Member, IEEE), NASSER AL-EMADI[1], (Member, IEEE), ANDRE ANTUNES[2], AND RICHARD BOWTELL[2]

[1]Electrical Engineering Department, College of Engineering, Qatar University, Doha 2713, Qatar
[2]Sir Peter Mansfield Imaging Centre, School of Physics and Astronomy, University of Nottingham, Nottingham NG7 2RD, U.K.
[3]Birmingham University Imaging Centre, School of Psychology, University of Birmingham, Birmingham B15 2TT, U.K.
[4]Advanced Medical Engineering Research Center, University of Hyogo, Kobe 650-0047, Japan

Corresponding author: Muhammad E. H. Chowdhury (mchowdhury@qu.edu.qa)

This work was supported in part by the Engineering and Physical Sciences Research Council (EPSRC) under Grant EP/J006823/1, in part by the Commonwealth Scholarship awarded to Muhammad E.H. Chowdhury, and in part by the Qatar National Library.

ABSTRACT The utility of EEG-fMRI is limited by the large artefact voltages produced in EEG recordings made during concurrent fMRI. Novel approaches for reducing the magnitude and variability of the artefacts are, therefore, required. One such approach involves using an EEG cap incorporating a reference layer (RL), which has similar conductivity to biological tissue and is electrically isolated from the scalp. The RL carries a secondary set of electrodes and leads that precisely overlay on the scalp electrodes so that similar voltages are anticipated to induce at the RL and scalp electrodes in the presence of static and time-varying magnetic fields. RL artefact subtraction (RLAS), which involves taking the difference of the voltages at the two electrodes, should, therefore, attenuate artefacts while leaving neuronal voltages unaffected. Previous experimental work has demonstrated the potential of the RLAS system in removing different types of EEG artefact. However, to get the best performance from the RLAS system, it is important to verify the underlying assumptions of RLAS and to optimize the RLAS system based on electromagnetic simulations. In this paper, electromagnetic modeling was used to simulate the voltages induced in a hemispherical RL and a spherical volume conductor (VC) under the influence of a static magnetic field and time-varying magnetic field gradient. By evaluating the differences in the voltages produced in the RL and VC, as the RL geometry is varied, the efficacy of the RLAS approach is tested and an optimal RL design is identified. The simulations performed accounted for realistic rotations, shifts, nodding, and shaking of the RLAS system with respect to the gradient isocentre, thus giving insight into the optimum RLAS set-up and the potential for improved EEG cap design for an RLAS system.

INDEX TERMS EEG artefact reduction, electromagnetic simulations, gradient artefact, reference layer artefact subtraction, simultaneous EEG-fMRI.

I. INTRODUCTION

Simultaneous electroencephalography (EEG) and functional magnetic resonance imaging (fMRI) is now a recognized tool for studying brain function [1]–[4] whose utility has been demonstrated in a number of areas including the study of resting state brain networks [3], [5], [6] and the non-invasive identification of epileptic activity [7]–[9].

The associate editor coordinating the review of this manuscript and approving it for publication was Fang Yang.

However, the successful implementation of simultaneous EEG-fMRI is severely hampered by the influence of the MR system on the EEG signal quality [10]–[13]. The main confounding factors are: i) the gradient artefact (GA), ii) the pulse artefact (PA), and iii) the motion artefact (MA). GAs are produced by the interaction of the temporally-varying magnetic field gradients with the EEG cabling and the electrically conducting structures in the human head [14], [15]. PA is caused by pulsatile motion with respect to the static magnetic field, B0, that is linked to the cardiac cycle [16]–[18]

whereas MA is caused by voluntary and involuntary head movements.

The GAs induced in the raw EEG data by standard fMRI sequences result in voltages, which are many orders of magnitude larger than the neuronal signals of interest. Correction of this artefact has previously been mainly carried out by using post-processing methods whose efficacy is limited, especially when subject movement occurs during data acquisition (for more detail see [19] and [20]). The PA although relatively periodic due to its link to the cardiac cycle, is variable in morphology across cardiac cycles [18]. This variability causes difficulty in PA correction using post-processing techniques, limiting their performance and resulting in residual PA that remains after post-processing. Finally, the MA is completely unpredictable both temporarily and spatially, making correction of this artefact using post-processing methods could be virtually impossible [21]–[23]. In addition, any changes in head pose also cause the morphology of the GA and PA to change leading to additional problems in correcting these artefacts using post-processing methods. The confounding effects of residual PA and MA on EEG-fMRI data was made clear in recent work that demonstrated the effects of spurious correlations between EEG and BOLD signals [24].

Recent studies by a number of groups have focused on monitoring head movement and using the resulting measurements to deduce the amount of PA and/or MA to be removed from the EEG data. Bonmassar *et al.* [25] attached a piezoelectric sensor to the subject's head to monitor head motion during combined EEG/fMRI experiments and then used a linear adaptive filter to remove any signal from the EEG recordings that was linearly related to the reference signal from the movement sensor. Masterton *et al.* [21] showed that the voltages induced in loops of carbon-fiber wire that were physically attached to, but electrically isolated from, the subject's head as a result of head movement in the static field of the MR scanner could also be used to ameliorate the PA and MA in post-processing. LeVan *et al.* [26] measured head movement using an optical camera and then used linear and quadratic functions of the measured motion parameters to correct the PA, although MA correction was not implemented in that work. Jorge *et al.* [22] implemented an approach similar to the one in Masterton *et al.* [21] by using wires to connect a few pairs of electrodes on the EEG cap thus creating wire loops. This approach is, however, limited in efficacy by the differences between the artefact voltages induced by complex head movement in the combination of the EEG leads and the volume conductor formed by the human head, and the signal from a limited number of motion sensors placed on the surface of an EEG cap attached to the head. All of these hardware solutions require fitting the measured motion signal to the voltages measured from the scalp electrodes, leading to the possibility of some neuronal activity being removed in the fitting process. In addition, none of these hardware solutions has addressed correction of the GA, and more particularly changes in the GA due to head movement.

The reference signal approach can be extended by using an EEG cap incorporating a reference layer (RL) comprising a second set of electrodes and leads that directly overlay those attached to the scalp [27], [28]. The reference layer is electrically conducting (with a similar conductivity to biological tissue), but is electrically isolated from the scalp so that the electrodes in this layer do not pick up brain signals. If it is assumed that the current paths formed by the reference layer and associated leads are very similar to those formed by the scalp leads and the head, similar voltages should be recorded from the scalp and reference layer leads in the presence of time-varying magnetic field gradients or head rotation. Taking the difference of the signals from associated reference layer and scalp leads should therefore cancel out the artefacts, but leave neuronal signals unaltered.

Author's previous work [28] demonstrated that the Reference Layer Artefact Subtraction (RLAS) approach could be used to reduce the gradient, pulse and movement artefacts in experiments carried out using a prototype system incorporating a small number of electrodes. A partial implementation of this approach in which a small subset of electrodes from the EEG cap are connected to a reference layer and used to detect the pulse artefact [12], [29] has also been described. In this approach, the PA measured from the ''reference electrodes'' is fitted to the PA occurring on all of the electrodes attached to the scalp.

Steyrl *et al.* [30] used the original RLAS approach with adaptive filtering (RLAF) where the reference layer electrode signals are not only subtracted from scalp electrode signals, but also adaptively scaled before subtraction. They have introduced a reference layer cap, which is equipped with mechanically tightly coupled and narrow spaced electrode pairs. The coupling ensures that electrodes of a pair can only move together, meaning that all electrode motion related artefacts are equally captured by both electrodes. Steyrl *et al.* [30] showed that RLAF and multi-band reference layer adaptive filtering (MBRLAF) both outperform RLAS and the most common artefact reduction method, average artefact subtraction (AAS).

The reference layer-based method showed great promise when implemented experimentally [28], [30], however the underlying assumptions for RLAS to work in the presence of time-varying field gradients or static magnetic field of the scanner have not yet been studied rigorously [31]. In the simple case of a reference layer forming a spherical shell surrounding a sphere, it can be shown that the voltages recorded from overlaying electrodes cancel perfectly (see [17], [32]). However, when recording from the human head, the reference layer has to be truncated, forming something closer to a hemispherical shell, which could potentially change the pattern of induced electric fields, and thus the measured voltages can be significantly different. This idea works perfectly for a spherical layer on a conducting sphere, but we do not know the effect of truncating the RL on the head, and then displacing it from the head and varying its thickness.

The aim of this work, a part of first author's doctoral work [31], was therefore to simulate the artefacts induced in a hemispherical reference layer and a spherical volume conductor by time-varying magnetic field gradients and movements (equivalent to head nodding and shaking actions). This electromagnetic modeling allows us to test the theoretical efficacy of artefact correction that can be achieved by using RLAS [28], making the assumption that the voltages induced in leads attached to the associated reference layer and scalp electrodes can be made identical. A series of simulations were carried out on simple spherical volume conductor with isotropic conductivity to evaluate the differences in the voltage produced in the hemispherical reference layer conductor and volume conductor, while the reference layer and insulating layer geometry parameters were varied. In addition, the effect of positional changes of the reference layer relative to the volume conductor, and changes in the RLAS system by shifting in the transverse or longitudinal directions were simulated to understand the sensitivity of the RLAS system to initial position. Together, these simulations were designed to inform the optimal design of a RLAS cap and to identify any theoretical limits on the reduction in induced artefact that could be achieved with an RLAS set-up.

II. THEORY

To characterize the artefacts induced it is necessary to consider the theory relating the electric field induced in a conducting sphere and hemispherical reference layer (RL) to the imposed vector potential, and consequently to the external current distribution based on a quasi-static approximation of Maxwell's equations. The vector potential (**A**), scalar potential (Φ) and electric field (E) can be related by

$$\oiint \sigma(\boldsymbol{E}) \cdot d\boldsymbol{S} = 0$$
$$\Phi \oiint \sigma(-\frac{\partial \boldsymbol{A}}{dt} - \nabla) \cdot d\boldsymbol{S} = 0 \tag{1}$$

where σ is the conductivity, $dS{=}da.n$ is infinitesimal area element, $dS{=}da.n$, n is the vector orthogonal to the surface, S and the time derivative of the vector potential is $\partial A/dt$.

This is the governing equation considering the boundary condition that shows the component of the current density (and, therefore, the electric field) normal to the surface of the conductive object is zero. This relationship can be solved for the scalar potential using a finite difference approximation method. To calculate the induced electric field, we segment the volume into a cuboidal array of Np cells (also described as volume elements). Application of Eq. (1) to all the elements of the discretized mesh gives rise to a linear system of equations (Liu et al., 2003) that can be represented as

$$\mathrm{Cx} = \mathrm{b} \tag{2}$$

where x is a vector of potentials to be solved, b is a vector dependent on the external field, and C is a sparse matrix [33]. Total size of the problem is, $Np = Nx \times Ny \times Nz$, where *Nx, Ny and Nz* represent the number of voxels in the respective dimensions, containing the conductivity and connectivity information for each of the element's surfaces.

The vector potential, *A*, can be calculated from a gradient coil's wire paths [32], [34]–[36]. However, the head is usually positioned in the gradient coils' region of homogeneity, during combined EEG/fMRI; so, the simple analytic expressions using Coulomb gauge for the magnetic field and vector potential, corresponding to pure gradients, described by Bencsik *et al.* [35] and Yan *et al.* [15], can be employed. The vector potential produced by an x-gradient coil can be written as:

$$\boldsymbol{A}_x = -\frac{1}{2}G_x xy\boldsymbol{i} + \frac{1}{4}G_x\left(x^2 - y^2\right)\boldsymbol{j} + G_x yz\boldsymbol{k} \tag{3}$$

where G_x is the field gradient strength, and the magnetic field is given by:

$$\boldsymbol{B}_x = G_x z\boldsymbol{i} + G_x x\boldsymbol{k} \tag{4}$$

However, when considering rotation of homogeneous, rigid and uncharged spherical conductor centered at the origin and rotating about the x-axis (equivalent to nodding) with angular velocity, $\Omega = \Omega\boldsymbol{i}$, in a uniform magnetic field, $B = B\boldsymbol{k}$; the nodding term can be written as described by Liu *et al.* [37]:

$$\boldsymbol{v} = \boldsymbol{\Omega} \times \boldsymbol{r} = \Omega(-z\boldsymbol{j} + y\boldsymbol{k}); \boldsymbol{v} \times \boldsymbol{B} = -\Omega zB\boldsymbol{i} \tag{5}$$

and for rotation about z-axis (equivalent to shaking) with angular velocity $\Omega = \Omega$k,

$$\boldsymbol{v} = \boldsymbol{\Omega} \times \boldsymbol{r} = \Omega\left(-y\boldsymbol{i} + x\boldsymbol{j}\right);$$
$$\boldsymbol{v} \times \boldsymbol{B} = \Omega(x\boldsymbol{i} + y\boldsymbol{j})B \tag{6}$$

where r is the space vector.

Since there is a separation between the two electrodes placed on two conductors, the assumption that the cables connected to VC, RL electrodes are overlaying completely and are of equal length is inappropriate. It is therefore important to consider the small wire that runs between two electrodes on both the conductors [35] (Fig. 1B). The induced voltage can be calculated directly from the rate of change of flux linked by the wire loop, using

$$V = -\oint \frac{\delta A}{\delta t} dl \tag{7}$$

where, A is the vector potential, related to the magnetic field, B.

III. MODELING AND METHODS

A homogeneous, spherical volume conductor (VC) of 0.08m radius (mimicking the size of a human head) was used as a model system for calculating the electric fields induced in the human head by externally applied time-varying magnetic fields gradients. A hemispherical hollow conductor with a finite thickness and similar conductivity (average conductivity of scalp is $\sigma \approx 0.33$ S m^{-1} [37]) as the spherical VC was used as the RL conductor. A finite volume method (Np = 204×204×204 voxels, at 1mm resolution), based on

the quasi-static approximation of Maxwell's equations given by Equation. 1 was used in conjunction with an analytic form of the driving vector potential described. The resulting linear system of equations given by Equation 2 was solved using the bi-conjugate gradient stabilized method, often abbreviated as BiCGSTAB algorithm [38]. It is a variant of the bi-conjugate gradient method (BiCG) and has faster, smoother convergence than the original BiCG.

In this study, the unknown scalar potential ϕ has been calculated using the known conductivity, σ and the time derivative of the vector potential, $\partial A/\partial t$. Once the equations have been solved for ϕ, the current density can be found by taking $J = -\sigma\nabla\Phi$. The BiCGSTAB algorithm's stopping criterion for convergence was a residual less than 10^{-10}. The algorithm execution is highly parallelizable, so C++ code [33] was used to take advantage of this feature.

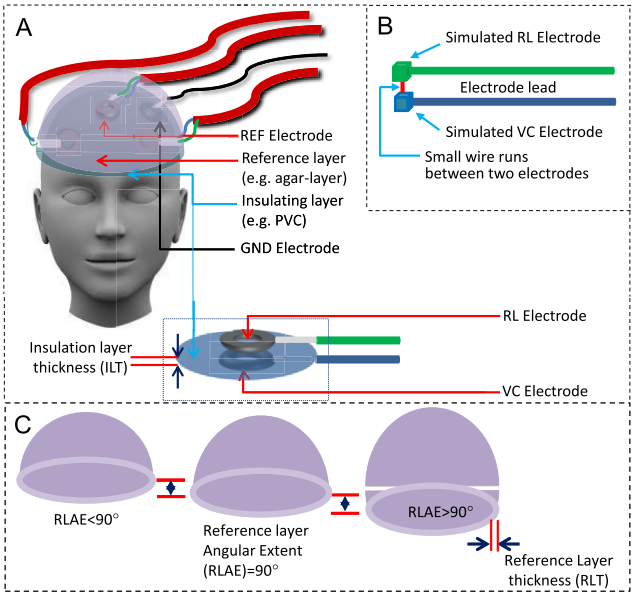

FIGURE 1. Schematic representations of the RLAS system experimental setup (A), Simulated VC and RL electrode with small wire running between them (B) and RLAS parameters (C). Proposed electrode set-up on VC and RL with insulating layer separating the electrodes (insert (A)).

The RLAS cap geometry used in all the simulations is shown in Figure 1, with the insert showing the simulated wire configuration, assuming perfect cancellation in the wires after they have been brought together. The wires connecting the VC and RL electrodes were simulated to have a radial orientation, relative to the sphere, ensuring the VC and RL electrodes were directly above one another. The key parameters which are defined and investigated to identify an optimal RLAS cap design are the reference layer thickness (RLT), insulating layer thickness (ILT) and reference layer angular extent (RLAE) [90° = hemisphere; 180° = sphere]. The inner radius of the RL depends on the ILT and the depth and separation of the VC and RL electrodes.

For the following simulations to assess the effect voltages induced by varying the magnetic field (as performed by the gradients), we evaluated the peak voltage generated by a realistic transverse (right-left) gradient of 10mTm^{-1} amplitude varying at 1kHz ($\text{dG/dt\_peak} = 62\text{Tm}^{-1}\text{s}^{-1}$). The voltages were evaluated on the surface of the volume and reference layer conductors at 33 electrode locations, defined by the extended 10/20 system. The volume conductor (VC) was simulated to be at isocentre and electrode Cz positioned on z-axis. To minimize the separation between electrodes positioned on the VC and RL, the electrode locations were modeled to be within the outer surface of the spherical VC and within the inner surface of the RL conductor. This provides a similar set-up to that used in our practical implementation [28], with the subtle difference where in the experimental condition the electrodes have to lie on the outer surface of the VC and the inner surface of the RL. The electrodes were simulated to have contact with a single point on the VC and RL rather than an extended area (Fig. 1B). This was done to assure that the sampling points of the electrodes on VC and RL are on their surface. If the potential of several points were used as electrode potential, these one-electrode representing points have to be averaged to produce single electrode potential. However, single sample point still represents the electrode avoiding the necessity of calculating the average.

By simulating head rotation, the ability of RLAS to correct the MA and PA can be assessed, as the PA is believed primarily to be induced by head rotation [17], [18]. To evaluate the artefacts induced by a head rotation, the VC and RL of the RLAS system must be rotated in the static field. For a head nod, the rotation was simulated to be about the x-axis, whilst for a headshake, rotation was simulated about the z-axis. For both rotation simulations, an angle of 5 deg/s in the relevant direction was used.

The first simulation was carried out to verify the expected similarity between the induced voltages in a spherical VC and a hemispherical RL separately when a time-varying transverse magnetic field gradient is applied. In these initial simulations, the reference layer and insulating layer parameters were set as follows: *RLT=5mm, ILT=3mm and RLAE=90*^{0}. A realistic RLAS set-up was mimicked by modeling the head as a homogeneous spherical VC, which was separated from the hemispherical RL by a thin insulating layer (Figure 1) while a transverse field gradient was applied. This allowed the evaluation of the feasibility of the RLAS technique for artefact correction.

The following simulations were carried out with the realistic RLAS set-up to identify the optimum parameters for an RLAS system for both a time-varying transverse magnetic field gradient and rotation in a static magnetic field. The reference layer and insulating layer parameters were varied sequentially, with the optimum value from earlier parameters set in each case. The parameters were initially set to the previously used values (*RLT=5 mm, ILT=3 mm and RLAE=90°*).

Whilst applying a time-varying transverse field gradient the following cases were considered:

a. To assess the importance of electrode placement on each surface: the effect of 2° or 5° mismatch between sample locations on the VC and the RL,
b. To assess the importance of the coverage of the RL on the VC: RLAE varied from 75° to 155° in steps of 5°
c. To assess the importance of the separation between the RL and VC electrodes: ILT varied from 2 to 15 mm in steps of 1mm
d. To assess the importance of the thickness of the RL: RLT varied from 2 to 15 mm in steps of 1mm
e. To assess the importance of head angulation relative to the gradient applied: the entire system was rotated about the x-axis by ±15° in steps of 1°
f. To assess the effect of the RL and associated electrodes potentially being misaligned with the VC and associated electrodes: the RL and associated sampling points were rotated while the VC and its sampling points were not rotated. RL only, rotated about the x-axis by ±15° in steps of 1°
g. To assess the importance of head location: the RLAS system was shifted
   I. Longitudinally by ±15 cm in steps of 1cm
   II. Transversally by ±15 cm in steps of 1cm

Whilst simulating head rotation about the x-axis and z-axis the following cases were considered:

h. RLAE varied from 75° to 180° in steps of 5°

In each of the above cases, the induced voltages were evaluated at the same 33 electrode locations on the VC and RL. To investigate the effect of translation on the induced GA from the transverse gradient, it was found to be easier to implement the effect translation of the RLAS system, by translating the gradient field rather than moving the RLAS system itself in the simulations. However, during the investigation of positional changes caused by rotation, the RLAS system was rotated rather than rotating the gradient field. Finally, for the simulations to study the induced voltages due to head rotation in the static field the RLAS system was rotated.

IV. ANALYSIS

The calculation of scalar potential and the time-derivative of vector potential are the time-consuming elements of the computation in this analytical study. At the problem size (204×204×204 voxels, at 1 mm resolution) chosen in this work, the calculation typically takes approximately 51minutes on a Core 2 Duo @ 3GHz 64-bit Windows machine (8 GB RAM installed), but this time reduces to 6 min when a Linux compiled version and GPU with 8 GB Memory, is used. Calculating the scalar potential alone or calculating the scalar potential along with the electric field and current density did not increase the computation time significantly. $\partial A/\partial t$ was generated, the conductivity map was plotted and the calculation of the induced voltage at the 33 sample locations (31 electrode locations, reference (REF) and ground (GND) electrodes) on the two conductors were done using an in-house written MATLAB code. C++ code [33] was used to calculate the scalar potential Φ, electric field E, and current density J. To implement RLAS, the potential values at the REF electrode locations on both the RL and VC were used for re-referencing the potentials measured at the 31 electrode locations on the respective conductors. For each case, the voltages at the VC and RL electrodes were found and the differences calculated. Line integration was calculated for the line between each VC and RL pair electrodes (Figure 1, Insert B), which were re-referenced using the line integral of REF electrode. The RMS amplitudes of the voltage difference between the VC, RL and re-referenced line integral as well as the voltages of the VC electrodes were calculated. Brain Vision Analyzer 2 (Version 2.0.1; Brain Products, Munich, Germany) and MATLAB were used for producing maps of the changes in RMS over the conducting surface.

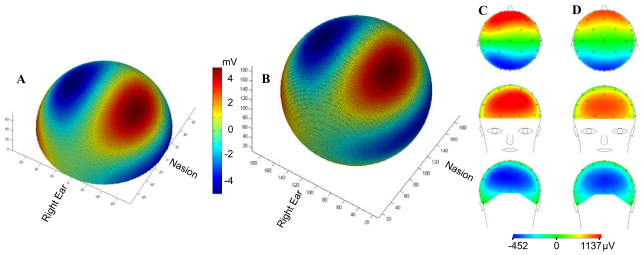

FIGURE 2. Potential distribution due to a time varying a transverse magnetic field for a hemispherical conducting RL (A) and spherical VC (B). Voltage maps for (C) for the line integration along the wires connecting electrodes and (D) the difference in induced voltages between the VC and RL. All plots are using the parameters: RLT=5mm, ILT=3mm and RLAE=90°. Note the difference in the scale of A&B compared with that in C&D and asymmetry in the scale of C & D.

V. RESULTS

A. EFFECT OF THE MISMATCH IN SAMPLING LOCATIONS OF VC AND RL

Figures 2 A&B show the potential distributions produced by a time-varying transverse magnetic field gradient applied to a hemispherical RL and spherical VC, with electrode location Cz on both conductors lying on the z-axis. The strong similarity of the artefact voltages on the surface of the two conductors (which forms the basis of RLAS) is evident. The RMS over the 31 electrode positions of the potential induced on the VC and RL (*RLT=5 mm, ILT=3 mm and RLAE=90°*) was found to be 2210 μV and 2747 μV respectively. Whilst the RMS of the line integration, representing the wires connecting the electrodes on the two conductors (Fig. 2C), after re-referencing using the REF electrode, was found to be 595 μV. Subtraction of the RL voltages and wire contributions from the VC voltages produced an attenuation of 27 dB (remaining voltage RMS=100 μV) of the induced gradient artefact. The voltage map showing the difference between the induced voltages on the VC and RL, having accounted for the wire contribution, due to a time-varying transverse gradient for a realistic RLAS set-up is shown

in Figure 2D. Even having accounted for the voltages induced in the wires, difference plot indicates the electrodes that measure the largest induced voltages (Fig. 2A&B) provide the largest contribution to the artefact discrepancy between VC and RL, with the anterior electrodes exhibiting the largest residual artefact for the transverse gradient.

Given the close spatial agreement between the RL and VC voltages (as shown in Fig. 2) it is unsurprising that a small mismatch between sample locations produces a large difference in the measured artefact voltages. A 2° mismatch increased the residual RMS from 100 μV (no mismatch) to 144 μV, whilst a 5° mismatch of the electrodes on the two conductors resulted in a residual RMS of 290 μV after subtracting the measured voltages on the two layers. This result clearly demonstrates that the sampling locations must overlay precisely.

B. EFFECT OF THE RL AND IL GEOMETRY PARAMETERS

Figure 3 shows how the RMS of the difference of the artefact voltages between the RL and VC electrodes varies for the range of RL and insulation layer (IL) geometry parameters investigated when a transverse magnetic field is applied. Figure 3A shows the effect of varying RLAE, which effectively changed the coverage of the RL over the VC. This figure shows that the minimum discrepancy between induced voltages is achieved when RLAE is equal to 90° (equivalent to a hemisphere), as used in our initial set-up shown in Figure 2. Varying ILT (RLAE=90°, RLT=5 mm) produces an almost linear increase in the RMS of the voltages induced in the simulated wire between the VC and RL across all electrode pairs (Fig. 3B insert). This is perhaps intuitive given the length of the wire has to increase with the increase of ILT to make sure the electrodes are still connected. However, because of this wire contribution, the difference in the induced voltages between two conductors does not significantly change with increasing ILT (Fig. 3B). The RMS potential difference is increasing with the increase of ILT; however, this is not a smooth increase as may have been predicted. This may have been resulted because of the 1mm step of ILT. If the simulation could be carried out with the step of ILT less than 1mm, the smoothness might increase. The best reduction in the induced gradient artefact (RMS=75 μV, 29 dB attenuation) is observed at the lowest ILT value (as shown in Fig. 3B). Fig. 3C shows that the discrepancy in the induced voltage is further reduced (RMS=34 μV, 36 dB attenuation) by increasing the RLT. In this simulation study, we have used RLT up to a thickness of 14 mm. However, this RLT value is not feasible for practical implementation and therefore RLT of 5mm was chosen as a trade-off between optimal performance and feasibility in implementation, since the gain of increasing RLT rapidly diminishes after 5mm. For a RLT<3 mm, the RMS discrepancy increases rapidly suggesting the RL no longer mimics the conductivity profile of the VC.

Figure 4 shows the artefact maps for the difference in induced voltages with different RLAS geometry profile parameters. The distribution of the difference in voltages

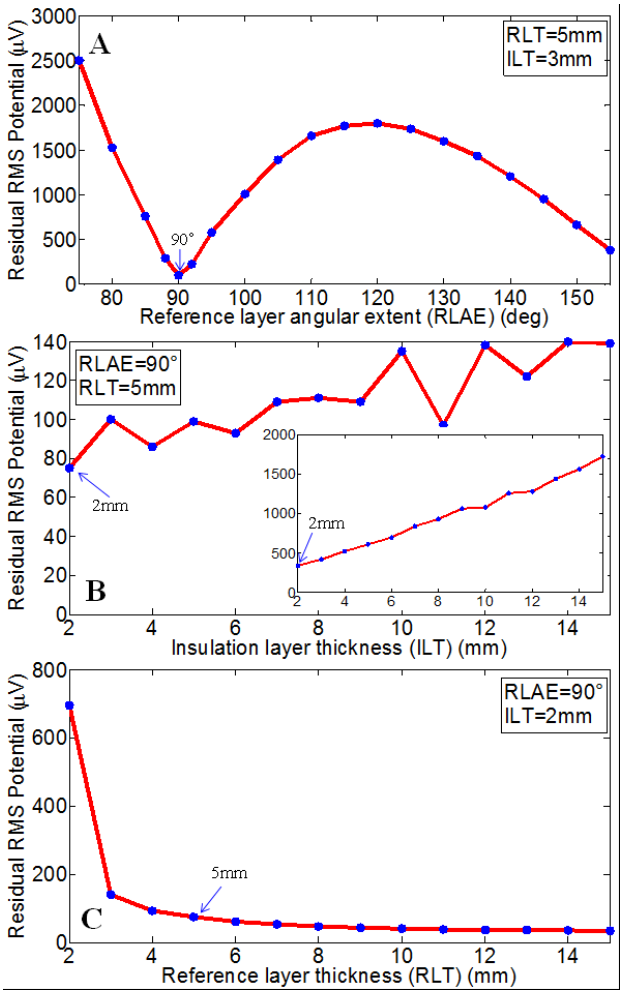

FIGURE 3. RMS of the difference in induced voltages between the VC and RL over sample locations for a range of reference and insulation-layer geometry parameters. Varying: A) RLAE, B) ILT and C) RLT. RMS of the line integration over sample locations for the line between VC and RL sample locations (Insert (B)).

between the conductors can be seen in Figure 4A, for the original set-up. It is clear from Figure 4A&B that the difference in the induced artefact voltage decreased considerably in the frontal and occipital lobes by reducing the ILT. Figure 4C shows that the frontal and occipital lobes electrodes mainly contribute to the artefact difference between RL and VC for the optimized RL and IL geometry parameters. From these simulations, we concluded that the RLAS system exhibits the optimum performance while retaining feasibility in practical implementation for a transverse varying magnetic field for the following geometry parameters: RLT=5 mm, ILT=2 mm and RLAE=90°.

C. EFFECT OF ROTATION OF THE RLAS SYSTEM

Figure 5 depicts the effect of rotation of the RLAS system in attenuating the artefact in the presence of transverse gradient. Firstly, the rotation of the RL, and associated electrode positions are creating mismatch between electrode locations on

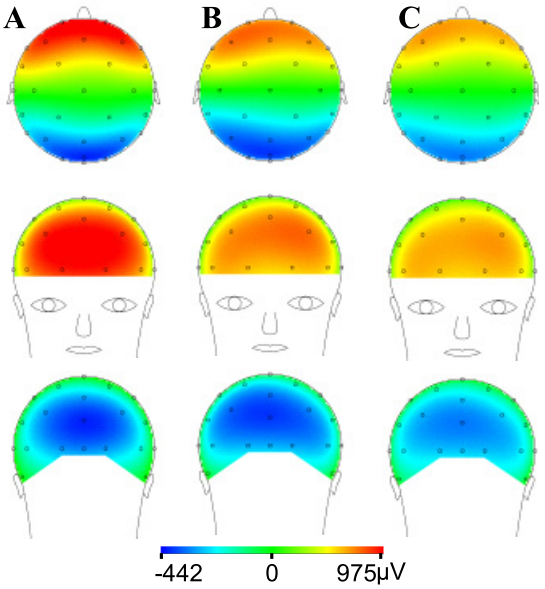

FIGURE 4. Artefact map for the difference in induced voltages between the VC and RL for (A) RLT=5mm, ILT=3mm and RLAE=90° (as shown in Fig. 2D but on a different scale), (B) RLT=5mm, ILT=2mm and RLAE=90° and (C) RLT=14mm, ILT=2mm and RLAE=90°.

the VC and RL, relative to the VC as the VC electrodes are not moving and only RL electrodes are moving (Fig. 5A-C). This simulation shows that no further improvement in the artefact attenuation can be achieved by rotating the system away from Cz being positioned on the z-axis (Fig. 5C). Fig. 5A shows that the RMS of the induced potential on the VC remains almost stable between the angle of rotations tested in this study with the minimum on the VC at $+5°$ (2205 μV). Fig. 5B shows that the difference between the conductors increases almost linearly with movement away from 0°, however positive and negative movements are not identical. Figure 5C shows that it does not produce any further reduction in artefact attenuation. Secondly, Figure 5D-F are showing the effect of the rotation of the RLAS system, when the RLAS system is rotated about the x-axis (the most plausible rotation of the head) while the transverse gradient is applied. Figure 5D shows that there is a pronounced effect on the voltages sampled from the VC through rotation of the RLAS system relative to the transverse field gradient. This result is in agreement with the previous simulation work of Yan *et al.* [15]. RMS of the induced voltage on the VC varies almost linearly between $-15°$ and $+5°$ with the minimum on the VC at $+5°$ (2051 μV). However, the difference in RMS potential between two conductors is almost independent of rotation (Fig. 5E) and the artefact attenuation is maximum at isocentre (RMS VC = 2275 μV, RMS difference = 75 μV and attenuation = 30 dB) (Figure. 5F). It is apparent that the variation in attenuation is only a few dB and therefore the RLAS system will perform well at removing the GA even if there is a change in head position due to x-rotation during data acquisition.

Figures 6A&B show the measured induced artefact variation in the VC and the difference between the VC and RL conductor, respectively, when the RLAS system is translated in the x direction (right-left). It is evident from Figure 6B that the minimum artefact difference (75 μV) is obtained at isocentre where RMS of VC artefact voltage is minimal (2210 μV). Moreover, the artefact attenuation shown in Figure 6C showed the maximum value of attenuation found to be 30 dB (75 μV) at isocentre where the RMS for VC is 2285 μV. Figures 6D&E show the variation of RMS artefact for an anterior-posterior (AP) translation (y-translation) of the RLAS system. The RMS of the induced voltage of VC is smallest (2151 μV) when the RLAS system is shifted 1cm in the posterior direction (-1cm, Figure 6D). However, the lowest artefact difference (75 μV) is found at isocentre as shown in Figure 6E, which is also evident from artefact attenuation plot shown in Figure 6F. The RMS of the induced artefact variation for the VC while translating the RLAS system in the longitudinal direction (z-translation) is shown in Figure 6G. The lowest artefact voltage (1289 μV) for the VC is observed at 2cm shift in the foot direction ($-2cm$ *z-shift*). However, the artefact difference is again found to be minimal at 0cm foot-head-shift (Fig. 6H), which is also reflected in the attenuation values in Figure 6I.

D. EFFECT OF THE RLAS GEOMETRY PARAMETERS ON THE ABILITY TO ATTENUATE MOTION RELATED ARTEFACTS

Finally, we assess the effect of the RLAS geometry parameters on the ability to attenuate motion related artefacts. The voltages that are induced by rotation about x-axis (nodding) and z-axis (shaking) of the RLAS system in static magnetic field were calculated when the RLAE was varied. Figure 7 shows the induced artefact variation when the RLAS system is rotated about x-axis by an angle of 5°/s and RLAE varied between 75° and 180°. It is evident from Figure 7 that the minimum artefact difference (10 μV) is obtained when the RLAE = 170° or more, which is the equivalent of fully covering the VC with the RL. The RMS of the induced voltage of VC is 179 μV for all RLAEs, this results in a 27dB attenuation of the VC voltages by the RL when the RLAE = 170°. This RLAE value was found to be optimal (residual RMS potential = 74 μV, attenuation = 30 dB) for the application of the transverse gradient. In the other hand, at RLAE = 90°, 0 dB attenuation of the VC voltages would be achieved when the RLAS system is rotated about x-axis. This reduction in attenuation at RLAE = 90° can be due to the voltages induced at the edge of the RL (i.e. where the hemisphere stops). This boundary did not however affect the voltages induced in the RL when the rotation was about the z-axis and for all RLAEs tested, the RMS of the induced voltage of VC was 338 μV, and the RMS of the difference between the induced voltages of conductors was one (1) μV (corresponding to 51 dB attenuation) (not shown). Figure 8 shows the effect of moving the RL boundary (by varying RLAE) on the artefacts induced in the RL.

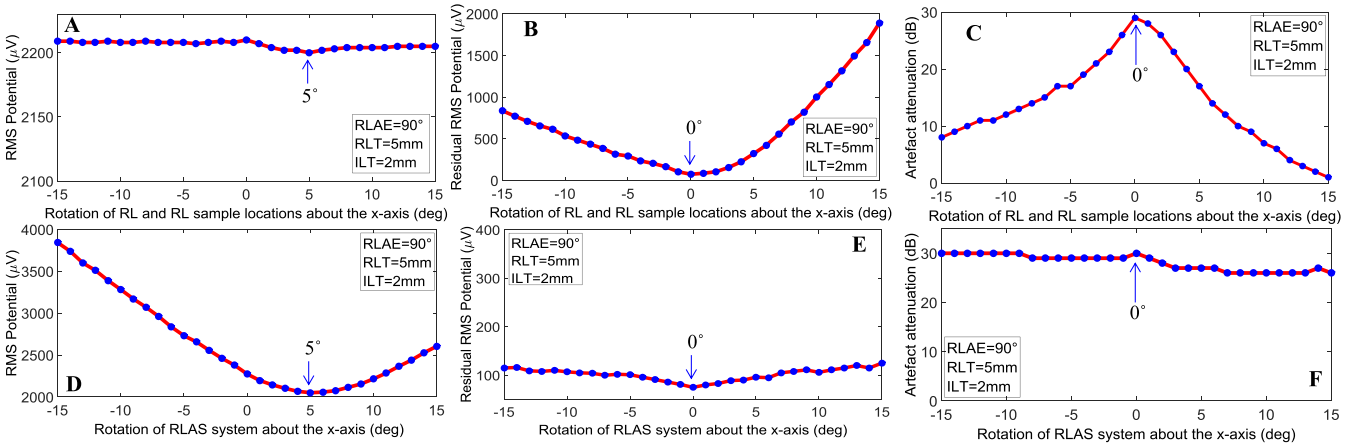

FIGURE 5. RMS of the induced voltage on VC (A & D) and the difference in induced voltages between the conductors (B & E) when RL and RL sample locations are rotated and RLAS system (VC, RL and all sample locations) is rotated respectively. Associated artefact attenuations for these rotations are shown in C & F where RLAE = 90°, RLT = 5mm, ILT = 2mm.

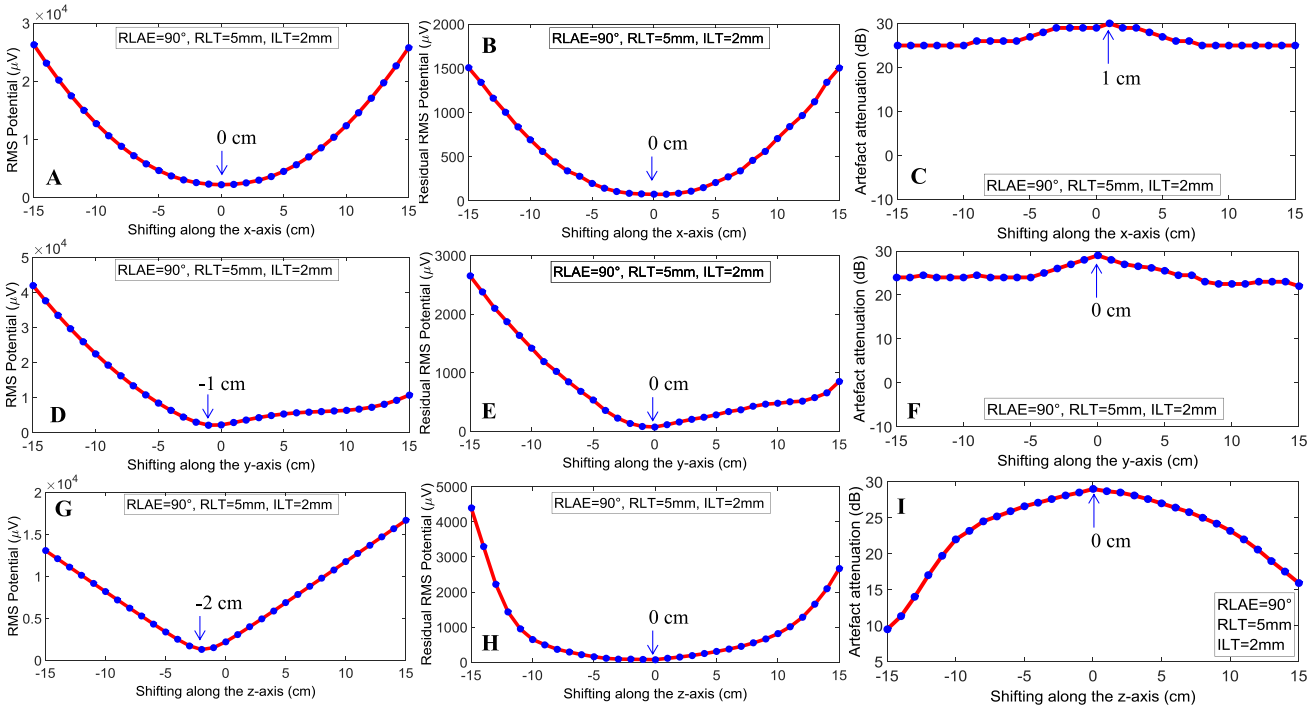

FIGURE 6. RMS of the induced voltage on VC (A, D & G) and the difference in induced voltages between conductors (B, E & H) when RLAS system translated along the x, y and z-axis respectively. Associated artefact attenuations for these translations are shown in C, F & I.

VI. DISCUSSION

Initial simulation results from realistic reference layer system (*RLT=5 mm, ILT=3 mm and RLAE=90°*) indicate that RLAS provides a viable method for attenuating the artefacts at source that are generated in EEG-fMRI experiments by time-varying magnetic field gradients. The results of preliminary experiments (Figure. 2) demonstrate that in the modeled system, consisting of a separate conducting sphere and hemispherical reference layer, potential distributions resulting from a time-varying transverse gradient are very similar in both conductors. Consequently, there is great potential in applying the RLAS technique to reduce time-varying gradient artefacts, which was evident from the author's experimental work [28]. For the initial RL and IL geometry parameters, it can be seen from Figure. 2 that the areas where the largest artefacts were induced are very similar for both the spherical VC and hemispherical RL. Therefore, the subtraction of the two sets of voltages greatly attenuates the induced artefacts. For this initial set-up, RLAS resulted in an attenuation of 27 dB without any other post-processing. The potential distributions at the electrode positions were also mapped onto a head shape using Brain Vision Analyzer 2 and found to

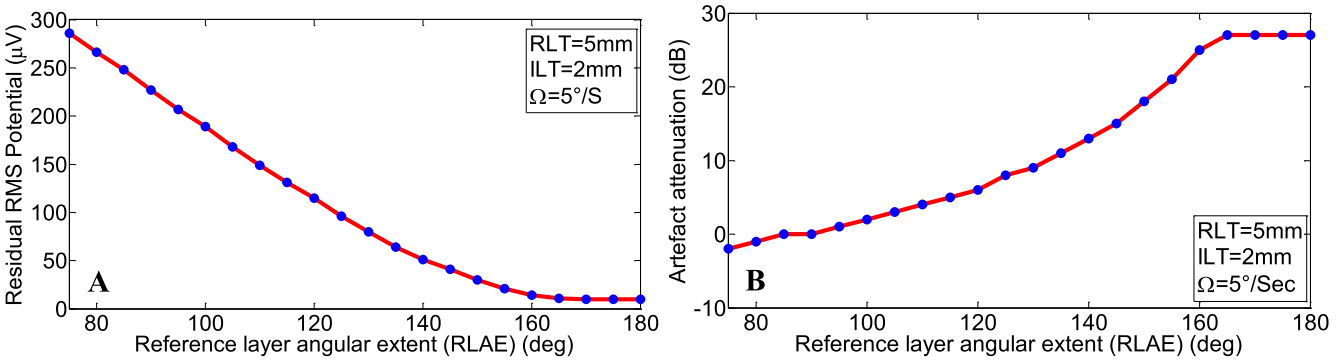

FIGURE 7. RMS artefact difference (A) and attenuation (B) of the induced voltages between conductors (VC-RL, accounting for the wire contribution) when RLAS system is rotated about the x-axis (nodding) by 5°/s in the presence of static magnetic field.

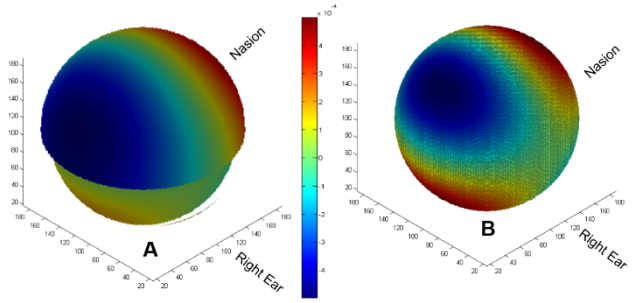

FIGURE 8. Potential distribution due to a static magnetic field for an RLAS set-up rotated about x-axis by 5°/s while the RLAE was (A) 90° and (B) 170° for RLT=5mm and ILT=2mm.

closely agree with previous work [15], which suggests the correct implementation of the computational methods used for these simulations. The line integration map, shown in Figure. 2C, shows that the potentials induced by the transverse gradient along the simulated wires connecting the electrodes also varies with spatial position, in a similar way to that on the VC and RL and therefore can serve to further reduce any differences in induced voltages between the two conductors. The difference map, shown in Figure 2D, depicts that the residual artefact is predominantly found in regions where the largest artefacts were induced, namely the occipital and frontal lobes. However, even in these regions, up to approximately a ten-fold reduction in the artefact amplitude can be achieved by taking the difference compared with the artefacts on the VC (Figure 2D compared with Figure 2A).

The close spatial agreement between the artefacts induced for both of the conductors means it is unsurprising that when there is a small mismatch between sample locations (i.e. electrode positions) between the VC and RL a larger difference in measured artefact voltages is obtained, than when the sample locations perfectly overlay one another. This was reflected in simulations where there was a 2°/5° of mismatch between the conductors' sample locations which caused an RMS discrepancy of 144/290 μV respectively; thereby reducing the artefact attenuation to 24/18 dB. Therefore, we conclude from these simulations that the sampling locations of the two conductors must overlay precisely to get the best results from the RLAS system.

The measure of the RMS of the difference in voltages induced in the RL and VC due to the time-varying transverse gradient provided a useful measure to investigate how to minimize the overall artefacts when geometry parameters of the RLAS system were changed. Variation of RLAE, which effectively changes the coverage of the RL over the VC, was found to affect greatly the level of residual artefact reduction that could be achieved by using RL. An RLAE of 90° (a hemisphere) was found to leave the least residual artefact with an RMS potential difference of 100 μV with small variations in this parameter causing sharp increases in the residuals. From Figure 2, we can hypothesize that the reason for the increase in residuals away from the optimum coverage is related to the boundary of the RL, the induced artefact increases when the boundary of RL fails to cover the electrode position properly. It is also unsurprising that when the RL is likely to have full coverage of the VC (i.e. a hollow sphere), then the RMS potential difference between the conductors is reduced again given that it is known that the voltages induced on the surface of a VC and hollow sphere are the same [32], [35]. Considering the variability of human head, this result therefore, also illustrates the necessity of making the RL from elastic material so that it can be adjusted on the subjects' head depending on their head shapes to optimize the RLAE.

It was assumed that the potential difference between the conductors would increase with ILT, since the increase in ILT causes an increase in RL radius. Therefore, the magnetic field experienced due to the time varying transverse magnetic gradient by the RL would be larger than that of the VC. However, simulation showed the RMS potential difference between the conductors, once the wire contribution was accounted for, shows very small variation of the residual potential difference with increasing ILT (Figure. 3B) with the best attenuation of 29dB achieved with an ILT=2mm (RLAE=90° and RLT=5 mm). Upon further investigation, the difference between hypothesis and simulation was found to be due to

the RMS of line integration increasing linearly with ILT (Figure. 3B, insert) because the wire length increased with increasing ILT and thus cancelled the majority of the effect of the increasing radius of the RL. Consequently, the ILT was found not to be as critical as expected, and an RLAS system should be designed to ensure proper insulation between the two conductors while the thickness of the insulation layer can be relatively flexible. It is however important to consider that a very thick insulation layer would still be undesirable as it may inhibit the normal evaporation from the head, which may increase localize temperature and can cause sweating and subsequent bridging of electrodes.

Reference layer thickness however does have significant effect on the difference in RMS potential that can be achieved. At an RLT of 3 mm or less, the discrepancy in the potential differences between the RL and VC rapidly increases. The first reason for this might be due to a limitation of the simulation, since the voxel size is 1mm^3, in the thin RL situations there were very few voxels that constitute the conductive path in the RL and therefore it is difficult to make a proper spatial distribution through this simulation. An alternative reason might be that the RL is no longer thick enough for voltages to be induced in it in the same way as they are in the VC. To test which of these were the case, for RLT = 3mm data were simulated with a 2mm^3 resolution and it was found that the difference in RMS potential was 429 μV instead of 150 μV with a 1mm^3 resolution, suggesting that the major source of the discrepancy was simulation limitation. It therefore can be suggested that by increasing the thickness of the RL, the layer acts more like a VC and hence the voltages induced in the RL become more similar to those of the VC. However, RLT=14mm is not practically feasible, and might cause undue heating of the subject. Therefore a RLT=5mm (ILT = 2 mm, RLAE = 90°), which produced an artefact discrepancy of 75 μV (29 dB attenuation), was deemed an optimal compromise between the practical requirements of the RL and the best performance in terms of artefact reduction.

The artefact maps, shown in Figure 4 display the effect of the RLAS geometry parameter variation on the spatial distribution of the residual induced potentials. When the initial parameters were used, the main artefact contributions come from the occipital and frontal lobe electrodes (Figure. 4A) whereas when the ILT is changed to 2mm, the occipital and frontal lobe electrodes' contributions were reduced (Figure. 4B). For RLT=14 mm, the artefact contribution was primarily from frontal and occipital lobe electrodes significantly reduced retaining asymmetrical distribution of residual induced potential.

It is important to consider possible rotations and translations of the RLAS system in the MR scanner since this allows the evaluation of the change in the induced gradient artefact, and residual gradient artefact, due to changes of head orientation and position. Understanding of these parameters will also help in optimizing the RLAS design and experimental set-up. In the case where the RL rotates (or slips) over the VC, the VC potential remains constant whereas the RL potential changes with angle of rotation (Figure. 5 A&B). Given the early results showing the need for electrode alignment, it is unsurprising that any deviation from the perfect overlaying of the layers and electrodes does not show any further improvement in artefact attenuation (Figure 5C). In contrast, rotation of the entire RLAS system about the x-axis reveals some interesting properties. Whilst it was predicted from Yan *et al.* [15] that the amplitude of the induced GA from the transverse gradient in the VC would change with angulation of the system, it was not known if the RLAS system would also perform uniformly at all angulations. Figure 5D shows the considerable variation in induced artefact with x-axis rotation and within the range of angles considered in these simulations showed that 5° produced the smallest artefact. However, the residual RMS potentials after the RLAS approach had been implemented were relatively stable (Figure 5E) for all angles, suggesting that the RLAS system will perform equally well at removing a transverse GA independent of the x-rotation of the head. This is particularly useful to know as it means that if a subject nods their head to a new position during a scan session, the transverse GA removal efficacy would be relatively independent of the movement or number of movements if RLAS was implemented; whereas conventional post-processing GA removal methods are affected by positional changes [39]. This result also suggests that implementation of post-processing methods, such as average artefact subtraction (AAS), to remove the residual GA after RLAS may perform better due to the independence of the residual artefact on head rotation. The difference of the induced artefacts in VC compared with the residuals after the application of RLAS for x-axis rotation were found to remain stable with rotation (Figure 5F).

Mullinger *et al.* [19] have showed that positioning subjects so that their nasion is displaced 4 cm axially from the scanner's isocentre towards the feet significantly reduces the gradient artefact produced by time-varying gradients applied in the RL and FH directions compared with the situation where the nasion is at the isocentre of the scanner. It has been shown that this decrease translates into a 40% reduction in the RMS amplitude of the gradient artefacts generated during conventional multi-slice EPI acquisition, used in the most EEG-fMRI experiments. This work emphasizes the importance of studying the positioning of the RLAS system inside the MR scanner. Figure 6 shows the effect of the transverse magnetic field gradient in inducing artefact voltages on the VC, the discrepancy between VC and RL and its attenuation by RLAS for the same axial shift of the RLAS system. The results of these simulations suggest that a 2cm axial shift from the scanner's isocentre towards the feet significantly reduces the VC RMS potential (Figure 6G). The RMS voltage of VC with a 2 cm shift toward the feet is 1289μV, which is almost two times smaller than that found at isocentre (2210 μV) (Figure. 6G). The discrepancy between the optimal position based on this simulation work and the previous experimental work could be due to a couple of differences. Firstly, the definition of where the shift is relative to is slightly different in the two cases: in the previous

experimental work, the shift was measured relative to the nasion whereas in this simulation work, the shift is relative to the center of the sphere. The more likely source of the discrepancy is that in these simulations the wire paths feeding from the electrodes to the amplifier were not accounted for (due to the nature of the RLAS system and assumed perfect cancellation of the artefacts in the wires of the VC and RL electrodes). Therefore, it is likely that the interaction of the voltages induced at the electrodes and in the wires of the conventional EEG system, used in the previous work [15], could be the reason of different amount shifts that were required in this simulation and previous experimental work by Mullinger *et al.* [19]. It might be expected that the difference between the VC and RL voltages might also be a minimum at this position. However, this is not found in the RLAS simulation where residuals are the smallest at 0cm shift in the z-axis, where the RMS artefact induced in VC and RL are 2210 and 2610 μV respectively, and the RMS difference is 75 μV, which offers 29dB artefact attenuation. This is far superior to the performance of single layer EEG system with 2cm shift towards the feet and further demonstrates the potential benefits of the RLAS system.

Movement of the RLAS system along the x- and y-axes, also was not found to improve the minimum residual artefact that could be achieved for the transverse gradient (Figures 6B&E). The attenuation performance of the RLAS system for the x-axis shifts was found to be relatively stable (Figure 6C). Although there is a slight improvement in attenuation when shifting 1cm toward the right (30dB compared with 29dB at isocentre), keeping the system at isocentre in all three planes would be the most feasible scenario for the RLAS system. Whilst achieving isocentre in the x- and z- axis is possible through careful subject positioning, this is more challenging in the y-axis (AP) since this is largely determined by the bed height and head size. For a Philips Achieva MRI scanner, the head coil surface where the back of the subject's head rests is positioned 6 cm away from the centre of the y-axis in the posterior direction. Therefore, assuming a head of radius 8cm (as used in this simulation study), this would result in 2cm posterior shift for the center of subject head compared with isocentre. This 2cm AP shift in the posterior direction will reduce the efficacy of the artefact removal by the RLAS system with a difference in RMS potential of 135 μV (compared with 75 μV at isocentre) corresponding to a reduction in attenuation to 20dB from 29dB. Therefore, the best performance of the RLAS system will be possible by lifting the head to ensure it is at isocentre. However, padding underneath the head will lift the head inside the coil, which is likely to have negative effects on the MR data quality. Experimental work is required to determine how to optimize this trade off within the practical limitations that are imposed by head coils.

Whilst the translation of the RLAS system from isocentre caused changes in the amplitude of the residual artefacts, the changes in these amplitudes were considerably smaller than the changes in the RMS potentials induced on the VC with positional changes. Therefore, along with the attenuation of the GA that the RLAS system itself can provide it will also help post-processing methods of correction as amplitude changes in the GA due to any movement will be smaller.

When considering the artefacts induced on the VC and RL by rotation of the system in the static magnetic field, it is important to find the simulation output when the system is rotated about the z-axis (shaking motion). In this case, a near perfect voltage cancelation could be achieved which was independent of RLAE once the wire contribution was accounted for (residual RMS potential is one μV; corresponding to 51 dB attenuation). This is in agreement with the analytical solution for this type of head rotation, and provides further verification that the computational processes used in the simulations are correct. This simulation therefore shows the high potential of the RLAS system to remove the effect of headshake motion from the EEG data. However, the simulations indicate that removing head nod artefacts using the RLAS system may be more challenging since the efficacy of the correction is dependent on the RLAE (Figures. 7&8). If the RLAE $= 90°$, the optimal value determined for the transverse gradient, no attenuation of head nod related artefact could be achieved (Figure 7B). This result can explain the experimental findings of the author (see in Figure 4, [28]) in the implementation of RLAS system for removing the head-nod. However, substantial attenuation (27dB) of the nodding artefact, which is similar to the best level of attenuation of the GA, can be achieved with a RLAE $= 170°$ or more. The reason for the large RLAE is related to the boundary of the RL and the voltages induced at this boundary. Due to the direction of the induced voltages caused by a head nod, large discrepancies are caused at the boundary edge. As already discussed, it is clear that a large RLAE will also work well to correct the GA (Figure. 2A) and therefore if a RLAE $=170°$ could be achieved then this could provide the best correction of all artefacts. However, due to the practical limitations of the human head with face and neck, this is clearly not possible. Further work must be done to determine the effect of gaps in the RL for the face if this might be a better solution for artefact correction than just having a smaller RLAE. This simulation may also highlight limitations of using the RLAS approach for correcting the pulse artefact, which is believed to originate predominantly from a head nod [17], [18], [40]. However, a number of groups have successfully implemented RL approaches for correcting the PA [28], [29], [41] and did not have unduly large RLAE in their set-ups, suggesting that there may be some discrepancy between these simulations and experimental findings for the head rotation, which require further investigation.

VII. CONCLUSION

The work described here has demonstrated the benefits in artefact reduction that RLAS can provide, but clearly, for these benefits to be widely realized, it is necessary to find the optimal reference layer configuration. The simulations performed accounted for realistic rotations, shifts, nodding

and shaking of the RLAS system with respect to the gradient isocentre, thus giving insight into the optimum RLAS set-up and the potential for improved EEG cap design for an RLAS system. This work suggests the optimal set-up for an RLAS system is RLT = 5 mm, ILT = 2 mm, RLAE = 90°. The RLAS system performance for GA correction was found to be relatively independent of rotation but it needs to be positioned at isocentre to give the lowest residual artefacts. Whilst the RLAS system was found to perform well for a shaking motion, a head nod was found to cause a challenge for the RLAS system since the performance of the system on this artefact required large RLAE. This simulation work suggests that RLAS is a viable method for removing artefacts in EEG data during simultaneous fMRI, and the RLAS approach should therefore be experimentally realized. However, the efficacy of the RLAS system is dependent upon the design of the system, thus, guidance from simulation work, will enable the best performance of an RLAS system to be realized. It is also important to note that using the RLAS system does not preclude the use of other post-processing methods to remove residual artefacts further, which can therefore lead to an even better reduction in residual artefacts in the EEG data

ACKNOWLEDGMENTS

All authors declare that the research was conducted in the absence of any commercial or financial relationships that could be construed as a potential conflict of interest. This manuscript was written based on the doctoral research [31] of Muhammad E. H. Chowdhury. However, the experimental findings were updated from the doctoral research based on his post-doctoral research work at Sir Peter Mansfield Imaging Center (SPMIC), University of Nottingham, U.K.

REFERENCES

[1] H. M. Khoo, N. V. Ellenrieder, N. Zazubovits, and F. Dubeau, "Epileptic networks in action: Synchrony between distant hemodynamic responses," *Ann. Neurol.*, vol. 82, no. 1, pp. 57–66, Jul. 2017.

[2] V. Zotev, M. Misaki, R. Phillips, C. K. Wong, and J. Bodurka, "Real-time fMRI neurofeedback of the mediodorsal and anterior thalamus enhances correlation between thalamic BOLD activity and alpha EEG rhythm," *Human Brain Mapping*, vol. 39, no. 2, pp. 1024–1042, Feb. 2018.

[3] H. Laufs, "A personalized history of EEG–fMRI integration," *Neuroimage*, vol. 62, no. 2, pp. 1056–1067, Aug. 2012.

[4] D. Mantini, L. Marzetti, M. Corbetta, G. L. Romani, and C. D. Gratta, "Multimodal integration of fMRI and EEG data for high spatial and temporal resolution analysis of brain networks," *Brain Topogr.*, vol. 23, no. 2, pp. 150–158, Jun. 2010.

[5] B. Feige *et at.*, "Distinctive time-lagged resting-state networks revealed by simultaneous EEG-fMRI," *Neuroimage*, vol. 145, pp. 1–10, Jan. 2017.

[6] S. P. Kyathanahally, Y. Wang, V. D. Calhoun, and G. Deshpande, "Investigation of true high frequency electrical substrates of fMRI-based resting state networks using parallel independent component analysis of simultaneous EEG/fMRI data," *Frontiers Neuroinform.*, vol. 11, p. 74, Feb. 2017.

[7] B. Ridley *et al.*, "Simultaneous intracranial EEG-fMRI shows inter-modality correlation in time-resolved connectivity within normal areas but not within epileptic regions," *Brain Topogr.*, vol. 30, no. 5, pp. 639–655, Sep. 2017.

[8] S. Markoula *et al.*, "The impact of mapping interictal discharges using EEG-fMRI on the epilepsy presurgical clinical decision making process: A prospective study," *Seizure*, vol. 61, pp. 30–37, Oct. 2018.

[9] R. Li *et al.*, "Epileptic discharge related functional connectivity within and between networks in benign epilepsy with centrotemporal spikes," *Int. J. Neural Syst.*, vol. 27, no. 7, 2017, Art. no. 1750018.

[10] C.-G. Bénar *et al.*, "Quality of EEG in simultaneous EEG-fMRI for epilepsy," *Clin. Neurophysiol.*, vol. 114, no. 3, pp. 569–580, Mar. 2003.

[11] I. Neuner, J. Arrubla, J. Felder, and N. J. Shah, "Simultaneous EEG–fMRI acquisition at low, high and ultra-high magnetic fields up to 9.4 T: Perspectives and challenges," *Neuroimage*, vol. 102, pp. 71–79, Nov. 2014.

[12] J. Jorge *et al.*, "Simultaneous EEG–fMRI at ultra-high field: Artifact prevention and safety assessment," *NeuroImage*, vol. 105, pp. 132–144, Jan. 2015.

[13] R. Abreu, A. Leal, and P. Figueiredo, "EEG-informed fMRI: A review of data analysis methods," *Frontiers Human Neurosci.*, vol. 12, p. 29, Feb. 2018.

[14] P. J. Allen, O. Josephs, and R. Turner, "A method for removing imaging artifact from continuous EEG recorded during functional MRI," *NeuroImage*, vol. 12, no. 2, pp. 230–239, Aug. 2000.

[15] W. X. Yan, K. J. Mullinger, M. T. Brookes, and R. Bowtell, "Understanding gradient artefacts in simultaneous EEG/fMRI," *NeuroImage*, vol. 46, no. 2, pp. 459–471, Jun. 2009.

[16] S. Debener *et al.*, "Improved quality of auditory event-related potentials recorded simultaneously with 3-T fMRI: Removal of the ballistocardiogram artefact," *NeuroImage*, vol. 34, no. 2, pp. 587–597, Jan. 2007.

[17] W, X. Yan, K. J. Mullinge, G. B. Geirsdottir, and R. Bowtell, "Physical modeling of pulse artefact sources in simultaneous EEG/fMRI," *Human Brain Mapping*, vol. 31, no. 4, pp. 604–620, Apr. 2010.

[18] K. J. Mullinger, J. Havenhand, and R. Bowtell, "Identifying the sources of the pulse artefact in EEG recordings made inside an MR scanner," *NeuroImage*, vol. 71, pp. 75–83, May 2013.

[19] K. J. Mullinger, W. X. Yan, and R. Bowtell, "Reducing the gradient artefact in simultaneous EEG-fMRI by adjusting the subject's axial position," *NeuroImage*, vol. 54, no. 3, pp. 1942–1950, Feb. 2011.

[20] M. E. H. Chowdhury, A. Khandakar, B. Hossain, and K. Alzoubi, "Effects of the phantom shape on the gradient artefact of electroencephalography (EEG) data in simultaneous EEG–fMRI," *Appl. Sci.*, vol. 8, no. 10, p. 1969, Oct. 2018.

[21] R. A. J. Masterton, D. F. Abbott, S. W. Fleming, and G. D. Jackson, "Measurement and reduction of motion and ballistocardiogram artefacts from simultaneous EEG and fMRI recordings," *NeuroImage*, vol. 37, pp. 202–211, Aug. 2007.

[22] J. Jorge, F. Grouiller, R. Gruetter, W. van der Zwaag, and P. Figueiredo, "Towards high-quality simultaneous EEG-fMRI at 7 T: Detection and reduction of EEG artifacts due to head motion," *NeuroImage*, vol. 120, pp. 143–153, Oct. 2015.

[23] J. N. van der Meer, M. A. J. Tijssen, L. J. Bour, A. F. van Rootselaar, and A. J. Nederveen, "Robust EMG–fMRI artifact reduction for motion (FARM)," *Clin. Neurophysiol.*, vol. 121, no. 5, pp. 766–776, May 2010.

[24] M. Jansen *et al.*, "Motion-related artefacts in EEG predict neuronally plausible patterns of activation in fMRI data," *NeuroImage*, vol. 59, no. 1, pp. 261–270, Jan. 2012.

[25] G. Bonmassar *et al.*, "Motion and ballistocardiogram artifact removal for interleaved recording of EEG and EPs during MRI," *NeuroImage*, vol. 16, no. 4, pp. 1127–1141, Aug. 2002.

[26] P. LeVan, J. Maclaren, M. Herbst, R. Sostheim, M. Zaitsev, and J. Hennig, "Ballistocardiographic artifact removal from simultaneous EEG-fMRI using an optical motion-tracking system," *NeuroImage*, vol. 75, pp. 1–11, Jul. 2013.

[27] W. Dunseath, "Electrode cap for obtaining electrophysiological measurement signals from head of subject, has measurement signal electrodes extended through electrically conductive layer and insulating layer for contacting head of subject," U.S. Patent 99 473 A, Feb. 2, 2009.

[28] M. E. H. Chowdhury, K. J. Mullinger, P. Glover, and R. Bowtell, "Reference layer artefact subtraction (RLAS): A novel method of minimizing EEG artefacts during simultaneous fMRI," *NeuroImage*, vol. 84, pp. 307–319, Jan. 2014.

[29] H. Xia, D. Ruan, and M. S. Cohen, "Separation and reconstruction of BCG and EEG signals during continuous EEG and fMRI recordings," *Frontiers Neurosci.*, vol. 8, p. 163, Jun. 2014.

[30] D. Steyrl, G. Krausz, K. Koschutn, G. Edlinge, and G. R. Müller-Putz, "Reference layer adaptive filtering (RLAF) for EEG artifact reduction in simultaneous EEG-fMRI," *J. Neural Eng.*, vol. 14, no. 2, p. 026003, Feb. 2017.

[31] M. E. H. Chowdhury, "Simultaneous EEG-fMRI: Novel methods for EEG artefacts reduction at source," M.S. thesis, Univ. Nottingham, Nottingham, U.K., 2014.
[32] M. Bencsik, R. Bowtell, and R. Bowley, "Electric fields induced in the human body by time-varying magnetic field gradients in MRI: Numerical calculations and correlation analysis," *Phys. Med. Biol.*, vol. 52, no. 9, p. 2337, Apr. 2007.
[33] A. Antunes, P. M. Glove, Y. Li, O. S. Mian, and B. L. Day, "Magnetic field effects on the vestibular system: Calculation of the pressure on the cupula due to ionic current-induced Lorentz force," *Phys. Med. Biol.*, vol. 57, no. 14, p. 4477, Jun. 2012.
[34] R. Bowtell and R. Bowley, "Analytic calculations of the E-fields induced by time-varying magnetic fields generated by cylindrical gradient coils," *Magn. Reson. Med. Off. J. Int. Soc. Magn. Reson. Med.*, vol. 44, no. 5, pp. 782–790, Nov. 2000.
[35] M. Bencsik, R. Bowtell, and R. M. Bowley, "Electric fields induced in a spherical volume conductor by temporally varying magnetic field gradients," *Phys. Med. Biol.*, vol. 47, no. 4, p. 557, Feb. 2002.
[36] P. M. Glover and R. Bowtell, "Measurement of electric fields due to time-varying magnetic field gradients using dipole probes," *Phys. Med. Biol.*, vol. 52, no. 17, p. 5119, Aug. 2007.
[37] F. Liu, H. Zhao, and S. Crozier, "Calculation of electric fields induced by body and head motion in high-field MRI," *J. Magn. Reson.*, vol. 161, no. 1, pp. 99–107, Mar. 2003.
[38] H. A. van der Vorst, "BI-CGSTAB: A fast and smoothly converging variant of BI-CG for the solution of nonsymmetric linear systems," *SIAM J. Sci. Stat. Comput.*, vol. 13, no. 2, pp. 631–644, Mar. 1992.
[39] M. Moosmann, V. H. Schönfelde, K. Specht, R. Scheeringa, H. Nordby, and K. Hugdah, "Realignment parameter-informed artefact correction for simultaneous EEG–fMRI recordings," *NeuroImage*, vol. 45, no. 4, pp. 1144–1150, May 2009.
[40] S. Debener, K. J. Mullinge, R. K. Niazy, and R. W. Bowtell, "Properties of the ballistocardiogram artefact as revealed by EEG recordings at 1.5, 3 and 7 T static magnetic field strength," *Int. J. Psychophysiol.*, vol. 67, no. 3, pp. 189–199, Mar. 2008.
[41] Q. Luo, X. Huang, and G.H. Glover, "Ballistocardiogram artifact removal with a reference layer and standard EEG cap," *J. Neurosci. Methods*, vol. 233, pp. 137–149, Aug. 2014.

MUHAMMAD E. H. CHOWDHURY received the B.Sc. and M.Sc. degrees (Hons.) from the Department of Electrical and Electronics Engineering, University of Dhaka, Bangladesh, and the Ph.D. degree in biomedical instrumentation from the University of Nottingham, U.K. He was a Postdoctoral Research Fellow with the Sir Peter Mansfield Imaging Centre, University of Nottingham, U.K. He is currently a Lecturer with the Electrical Engineering Department, Qatar University. Prior to joining Qatar University, he worked in several universities of Bangladesh. His current research interests include biomedical instrumentation and signal processing, wireless body sensors, artificial intelligence and machine learning, embedded system design, and simultaneous EEG/fMRI. In these areas, he has published several peer-reviewed journal and conference papers. He has been involved in several external and internal grants, academic and government projects, EPSRC, and EPSRC/ACC along with national and international awards. His research experience focuses on combined electroencephalography and functional magnetic resonance imaging (MRI). This is a powerful approach to functional brain imaging which provides simultaneous measurements of electrical activity and blood flow changes in the brain. However, recording the weak voltages produced at the surface of the scalp by brain activity in the presence of the large time-varying magnetic fields that are used in MRI is technically challenging. He was a consultant for the projects entitled Driver Distraction Management Using Sensor Data Cloud (2013–2014, Information Society Innovation Fund Asia). He received the ISIF Asia Community Choice Award 2013 for project entitled Design and Development of Precision Agriculture Information System for Bangladesh.

AMITH KHANDAKAR received the B.Sc. degree in electronics and telecommunication engineering from North South University, Bangladesh, and the master's degree in computing (networking concentration) from Qatar University, in 2014. He graduated as the Valedictorian (President Gold Medal Recipient) of North South University. He is currently the General Secretary of the IEEE Qatar Section and also the Qatar University IEEE Student Branch Coordinator and an Adviser (Faculty). He is also a certified Project Management Professional and the Cisco Certified Network Administrator. He was a Teaching Assistant and Lab Instructor for two years for courses, such as mobile and wireless communication systems, principle of digital communications, introduction to communication, calculus and analytical geometry, and Verilog HDL: modeling, simulation and synthesis. Simultaneously, he was a Lab Instructor for the following courses: programming course "C," Verilog HDL, and general physics course. He has been with Qatar University, since 2010. After graduation, he was a Consultant in a reputed insurance company in Qatar and in a private company that is a sub-contractor to National Telecom Service Provider in Qatar.

KAREN MULLINGER received the B.Sc. degree in physics with a focus on medical physics from the University of Nottingham, and the Ph.D. degree from the Sir Peter Mansfield Magnetic Resonance Centre, University of Nottingham. Her Ph.D. addressed many aspects of simultaneous EEG-fMRI recordings, including improving EEG artefact correction, reducing artefacts at ultra-high field to make simultaneous recordings feasible, and identifying the major sources of MR image distortion due to EEG hardware. She has gained unique and wide-ranging experience in the development and application of simultaneous electroencephalography (EEG) and functional magnetic resonance imaging (fMRI) over the past seven years, while working with the first MR-compatible EEG system (from Brain Products, Germany) at SPMMRC, Nottingham. This has involved collaboration with academic and industrial research leaders (e.g., Brain Products and Philips Medical Systems). Subsequently, as a Sir Peter Mansfield Research Fellow and an Anne McLaren Research Fellow, she has played a leading role in research aimed at understanding the origins of the gradient and pulse artefacts in EEG data, as well as in the development of beamformer techniques for localizing EEG sources in EEG-fMRI experiments. She has established a number of collaborations with academic and industrial research leaders. The success of her work is reflected not only in her publication record but also in three personal invitations to contribute to book chapters. Additionally, she has been invited to speak at several international conferences. The importance of her contribution in advancing EEG-fMRI research was recognized by the award of the prestigious International Society of Magnetic Resonance in Medicine Junior Fellowship, in 2011. She is working as a joint Lecturer post between the University of Birmingham (Psychology) and the University of Nottingham (Physics). She is using this unique post to develop her research interests and facilitate collaborations between the universities.

BELAYAT HOSSAIN received the M.Sc. degree from the University of Dhaka, in 2011, and the Ph.D. degree from the Graduate School of Engineering, University of Hyogo, Japan, in 2018. He served as a Lecturer with the Atish Dipankar University of Science and Technology, Bangladesh from 2011 to 2013. He is currently a Postdoctoral Research Fellow with the Advanced Medical Engineering Research Center, Japan. His research interest includes biomedical signal and image analysis. He received the NSICT (BD) Fellowship, in 2010, the Best Paper Award from the 18th ISIS Conference, in 2017, and the Student Presentation Award from the Japan Society for Fuzzy Theory and Intelligent Informatics, in 2016. He has received the MEXT Scholarship for his graduate study. He is also an IEEE Student Member.

NASSER AL-EMADI received the B.Sc. and M.Sc. degrees in electrical engineering from Western Michigan University, Kalamazoo, MI, USA, in 1989 and 1994, respectively, and the Ph.D. degree from Michigan State University, East Lansing, MI, USA, in 2000. He is currently the Head and an Associate Professor with the Electrical Engineering Department, Qatar University, Doha, Qatar. He has a wide experience in electric power systems, control, and protection, and in sensor interfacing, control of multi-phase motor drives, and renewable energy sources, as well as the integration of smart grid. He has published widely in international conferences and journal papers in his field of expertise. He holds several patents. He has co-authored a book and two chapters in two other books. He has supervised several large R&D projects. He is a Founding Member of the Qatar Society of Engineers and a member of the IEEE and the Advisory Board of the IEEE Qatar section.

ANDRE ANTUNES received the Ph.D. degree from the University of Nottingham, in 2012. He was a Research Scientist with the Max Planck Institute for Biomedical Cybernetics, from 2012 to 2014. He has worked for the development and maintenance of simNIBS—a software package for automatic generation of head models for MR images and detailed electric field calculations, for use in, e.g., TMS and tDCS. He has developed algorithms to speed-up electric field calculations in head models. This allows a revolutionary real-time visualization of the electric field originated by TMS pulses in a realistic and personalized head model of the subject. He was an Algorithm Engineer with Medtronic, U.K.

RICHARD BOWTELL received a degree in natural science from the University of Cambridge and the Ph.D. degree from the University of Nottingham, in 1984, under the supervision of Sir P. Mansfield, the inventor of magnetic resonance imaging. He is the Head of the School of Physics and Astronomy, University of Nottingham. Having been appointed to the academic staff of the Department of Physics, in 1989, he was promoted to Reader in 1995 and to Chair in physics with the School of Physics and Astronomy, in 2000. His research is carried out at the Sir Peter Mansfield Magnetic Resonance Centre—a research Centre that houses two whole-body magnetic resonance imaging systems, including the highest field (7 T) system in the U.K. for imaging human subjects. His research focuses on developing improved equipment and techniques for magnetic resonance imaging and applying them in biomedical studies. He has a particular interest in spatio-topic mapping of human–brain function using ultra-high field MRI.